Algorithmic linearization improves Syringe-based extrusion in elastic systems using Hydrogel-based materials

Jernej Vajda [a,d], Luka Banović [b], Mihael Miško [b], Igor Drstvenšek [c], Marko Milojević [a,d], Uroš Maver [a,d], Boštjan Vihar [a,b,*]

[a] University of Maribor, Faculty of Medicine, Institute of Biomedical Sciences, Taborska ulica 8, 2000 Maribor, Slovenia
[b] IRNAS Ltd, Limbuška cesta 76b, 2000 Maribor, Slovenia
[c] University of Maribor, Faculty of Mechanical Engineering, Laboratory for additive manufacturing, Smetanova ulica 17, 2000 Maribor, Slovenia
[d] University of Maribor, Faculty of Medicine, Department of Pharmacology, Taborska ulica 8, 2000 Maribor, Slovenia

HIGHLIGHTS

- Accuracy and precision are essential for successful extrusion bioprinting, however, intrinsic properties of the components such as nozzle and cartridge shape, elasticity, backlash, etc. immensely complicate the predictability of the results.
- This work demonstrates an iterative optimization algorithm that introduces rapid piston movements to compensate for temporal discrepancies between piston motion and material extrusion.
- The developed approach allows process optimization without prior knowledge of set-up parameters and properties of the printing material, which makes it versatile and suitable for a wide range of applications. Particularly when the combined set-up and material properties are too complex for solely predictive approaches.
- The approach is based on repeated sequences of extrusion, continuous measurement of mass progression and adjustment of machine instructions that are generated by an algorithm developed in the Python programming language.

GRAPHICAL ABSTRACT
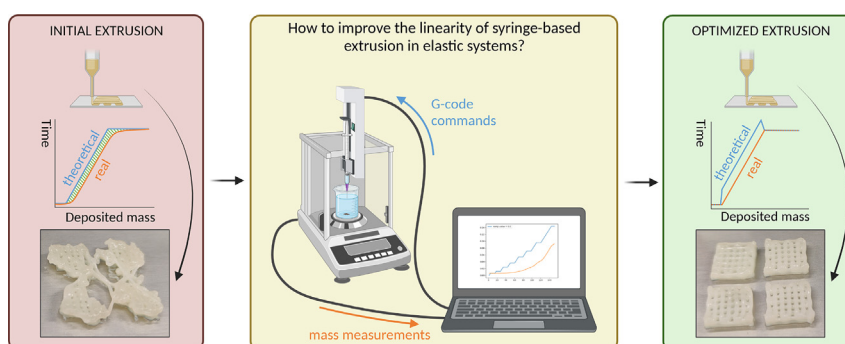
ARTICLE INFO

ABSTRACT

Accuracy and precision are essential in extrusion-based material handling such as three-dimensional (3D) bioprinting. However, the elasticity of components, backlash, variability of nozzle and cartridge

---

* Corresponding author at: University of Maribor, Faculty of Medicine, Taborska ulica 8, SI-2000 Maribor, Slovenia.
  E-mail address: bostjan.vihar@um.si (B. Vihar).

shapes, etc. can lead to unpredictable printing results, which is further complicated by the wide range of rheologically diverse materials and complex sample designs.

To address this issue, we present an algorithmic approach to compensate for the discrepancies between piston motion and material extrusion in syringe-based extrusion systems. This approach relies on cyclical, iterative optimization through rapid piston movements, which are adjusted based on extrusion analysis.

In this work we establish a general theoretical framework for extrusion and link the rheological properties of prepared hydrogels with shear rates in a typical bioprinting process. The determined properties are compared with the success of the developed algorithm to modify machine instructions for precise material deposition of short, interrupted lines, as well as multi-layered scaffold structures.

Overall, our approach provides a means of improving the accuracy and precision of complex extrusion-based bioprinting systems, without prior knowledge of set-up or material properties, making it highly versatile and suitable for a wide range of applications, particularly when the combined set-up and material properties are too complex for solely predictive approaches.

1. Introduction

Syringe based dosing systems have found many applications in physical, life sciences and engineering, including liquid handling, electro spinning and most recently (and perhaps most prominently) 3D bioprinting. As a highly versatile technology, the latter has become the focus of tissue engineering, regenerative medicine, and many other biomedical applications [1–3]. As a result, the adoption of this technology is rapidly increasing. This is not only seen from the number of published related papers (Fig. 1) but also from the increasing bioprinting market [3,4]. However, commercial solutions are expensive and often cannot be adequately adapted to the individual processes required to meet the diverse needs of researchers [5,6].

The advent of open-source microcontrollers and the availability of prototyping technologies have enabled the rapid development of hardware. The latter has also found its way into research, allowing scientists and educators to perform complex experiments at a lower cost while having a high degree of control over the process itself [7–10]. In this regard, bioprinters are not only no exception but perhaps even the epitome of customized research devices [5,6,11–16]. Some excellent publications have presented low-cost yet high-precision open-source bio-printers [6,13,17]. However, since the accuracy and precision of computer-aided manufacturing systems (CAM) (*e.g.*, 3D printers) are highly dependent on the tolerances of the components used in the manufacturing process, some variability between prototypes is expected. Since low-cost systems rely on motion control by stepper motors rather than direct regulation of travel (*e.g.*, by incremental measurement scales), other parameters, such as clearance between the spindle and nut or clearance between the syringe and fixture, can also contribute to extrusion resolution. All mentioned can significantly reduce the degree of precision and overall control [5,6]. Most extrusion-based piston-driven 3D printers use (modified) syringe pumps as the mechanism for material deposition. These typically rely on relatively soft disposable syringes [5,11–14,16,18], which are often connected to the nozzle via a hose attached to the 3D printer to reduce the weight of the moving extruder components and thus the load on the drive system [13,14,16]. However, research has shown that the mechanical properties of the syringe itself (*e.g.*, the elasticity of the piston) can play an important role in extrusion latency and reproducibility, especially when using high-viscosity inks that require high pressures to extrude [5]. Finding optimum extrusion parameters quickly is essential for bio-
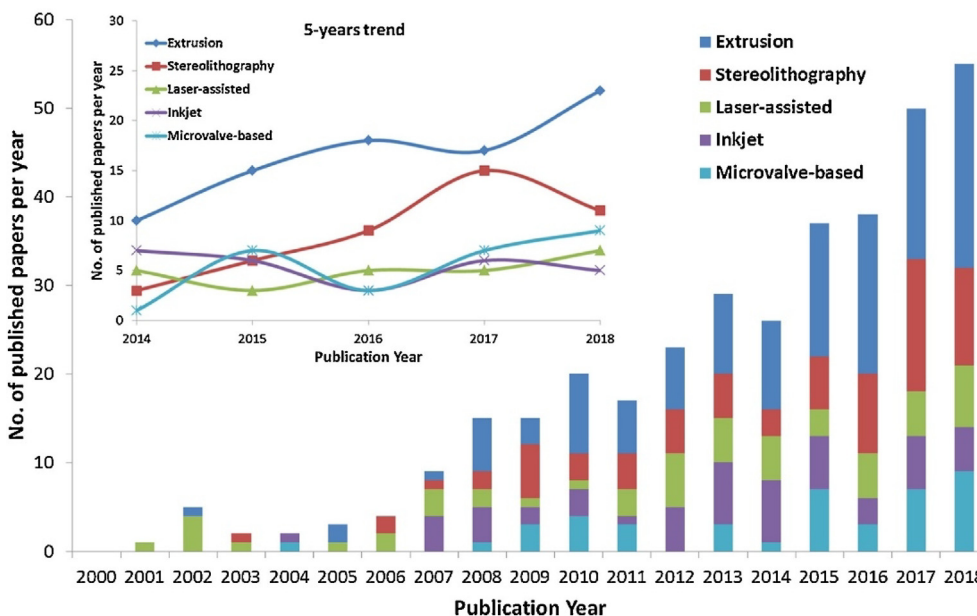

Fig. 1. Number of publications on 3D bioprinting since year 2000. Reprinted from Progress in Polymer Science, Wei Long Ng, Chee Kai Chua, Yu-Fang Shen, Print Me An Organ! Why We Are Not There Yet, Copyright (2019), with permission from Elsevier [3].

printing and other extrusion-based processes, especially when expensive and/or rare components are used in the process. Nevertheless, due to the variability of set-ups and application-specific requirements, this has been challenging in the past. Bonatti et al., 2021 have identified over 20 parameters that play a role in 3D bioprinting, related to the set-up, used materials and the process itself [19]. Different approaches have been developed for evaluating the 'printability' and optimizing the manufacturing process using mathematical modelling [19,20], machine learning [21] and the development of calibration methods [22,23]. This work demonstrates a detailed analysis of material extrusion as a function of "ink" viscosity, syringe and nozzle diameter, volume displacement, and feed rate. Based on the course of the mass flow as a function of the above parameters, an optimization of the motion instructions, *i.e.,* the NC code (ISO 6983), is proposed, which will significantly improve the quality of the final prints and can be used with different NC code formats. Most importantly, an experimental set-up and an optimization algorithm are demonstrated that help obtain the optimal printing parameters and are compatible with the equipment available in most biomedical research environments and with a wide range of bioprinting settings and software. In essence, the purpose of the proposed algorithm is adapting the cybernetic response without prior knowledge of the "ink's" material properties, eliminating the need for additional equipment and experiments and thus reducing the required time and cost of the optimization process of extrusion.

2. Materials and methods

2.1. Theoretical considerations of piston-driven extrusion

Consistent with the conservation of mass flow rate and the low compressibility of water, and consequently of hydrogel-based (bio) inks, it is reasonable to assume that the volume displaced by the movement of the piston in a syringe must be equal to the volume of material deposited. A schematic representation of the volume flow in a piston-driven extrusion system can be found in Fig. 2 and Equations (1)–(6). For a cylindrical syringe and a round extrusion nozzle with known dimensions, the displaced/deposited volume can be used in calculations to correlate the piston

Fig. 2. Schematic depiction of piston-driven extrusion. Piston movement (L) in the syringe with an internal diameter (D) displaces a volume of the material (V_s) to form a filament of volume Vf, with a length l and height h.

movement (L) and the syringe diameter (D) with the length (l) and diameter (d) of the deposited (cylindrical) filament. Under ideal conditions, the volume of material displaced in the syringe (V_s) as calculated in Equation (1) is equal to the volume of deposited filament (V_f) calculated in Equation (2).

$$V_s = \pi L \left(\frac{D}{2}\right)^2 \tag{1}$$

$$V_f = \pi l \left(\frac{d}{2}\right)^2 \tag{2}$$

Extrusion-based 3D printing is a process in which the material is deposited while the nozzle is in relative motion to the target surface. For CNC machines, the motion is coded with 3 or more axes (X, Y, Z), and the feed rate (f) describes the speed of the motion, usually in mm/min. Here, f is the speed of the combined motion path over all axes, calculated using the Euclidean approach (Equation (3)).

$$f = \frac{\sqrt{l^2 + L^2}}{t} \tag{3}$$

Assuming that V_s equals V_f, the internal dimensions of the syringe can be correlated with the dimensions of the deposited filament (Equation (4)). Since the relationship between the feed rate (f) and its extrusion component (f_L) is equal to the ratio of l to L (Equation (5)), the theoretical displacement of the piston can be expressed as shown in Equation (6).

$$L = \frac{ld^2}{D^2} \tag{4}$$

$$\frac{f_L}{f} = \frac{L}{l} \tag{5}$$

$$f_L = f \frac{d^2}{D^2} \tag{6}$$

2.2. Extrusion progression in elastic piston-based systems

In a motor-driven extrusion system, the motor axis rotation is converted into linear motion and displacement of the piston, resulting in the extrusion of material from the syringe through the nozzle. The flow of material in this process is affected by the fluid's viscosity and the shear rate in the syringe. The shear rate is the speed at which layers or lamellae of fluid move past each other. It is determined by the channel or tube shape, and the flow velocity v. Assuming a cylindrical shape of the syringe, the fluid's shear rate in the syringe is represented by Equation (7).

$$\dot{\gamma} = \frac{8v}{D} \tag{7}$$

The viscosity η is the ratio between the shear stress τ and the shear rate γ (Equation (8)), and therefore defines the force required to push the piston of the syringe to extract the defined fraction of material through the nozzle.

$$\tau = \eta \dot{\gamma} \tag{8}$$

The linear fluid velocity v in the syringe or nozzle is related to the volumetric flow rate Q and the syringe/nozzle cross-section area as shown in Equation (9), where r is the radius of the syringe or nozzle.
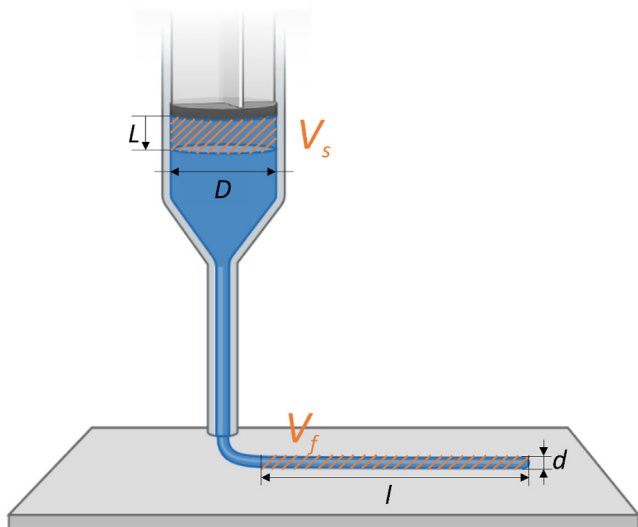
$$v = \frac{Q}{\pi r^2} \tag{9}$$

The shear rate within the syringe nozzle can thus be expressed using the Hagen-Poiseuille equation:

$$\dot{\gamma} = \frac{4V}{\pi r^3 t} \tag{10}$$

Allowing the equation for shear stress to be written as follows:

$$\tau = \eta \frac{4Q}{\pi r^3} \tag{11}$$

This very simplified explanation shows that the difference between the syringe diameter and the nozzle diameter plays an important role in the deposition of the material. The force required to push the ink through the nozzle creates the pressure inside the extrusion system (syringe and nozzle), which causes its elastic deformation and thus affects the flow of the ink. This role becomes even more important when considering the non-Newtonian behavior of most fluids used in bioprinting applications. Shear-thinning is the behavior of non-Newtonian fluids whose viscosity decreases under shear stress. Therefore, the above equations must account for the variable nature of viscosity by applying one of the shear-thinning models described by [24] and [25]. Ideally, the material flow should be linear to the piston displacement as described above. However, in systems containing soft and elastic components, such as disposable syringes, tubing, *etc.*, some of the energy is transferred to the elastic deformation of the components. In addition, the presence of air bubbles in the material or the syringe in general (due to imperfect methods of preparing the material and filling the syringe with the material) can have a large effect on the elasticity of the entire system due to the compressive properties of air. The deformation of the system is caused by the pressure generated by the force that moves the piston and corresponds to the shear stress inside the fluid to be dispensed. In addition, the material is subject to shear thinning, which is velocity and shape-dependent. Shear-thinning is believed to be due to small structural changes within the fluid [26] and has been characterized for polymer based and particle containing materials [27]. We can assume that the influential factors besides the elastic deformation mentioned above could be the structural changes and even phase transformations within the material, some of which are irreversible [28]. Moreover, extrusion-based bioprinting as well as filament based (FDM) printing relies on using a variety of materials with different viscoelastic properties [1–3]. Hence it seems unreasonable to construct an applicable theoretical viscous flow model for each hardware/material combination. Also, it is inconvenient as it makes the whole process practically impossible. Therefore, we have developed a sustainable empirical way to ensure uniform material distribution in extrusion-based 3D printing systems. It defines the viscoelastic properties of the hardware/material combination used by measuring the time dependence of the mass flow through the extruder. The resulting material flow parameters are then used in the preparation phase of the printing process. A comparison of the ideal and real flow in an elastic extrusion system is shown in Fig. 3. The measured mass flow curve (orange) starts with a transition phase (exponential). The flow gradually increases to reach a slope parallel to the ideal curve and continues until the piston motion is stopped. At this point, the extruded mass in the measured curve is below the ideal values. Still, it continues to increase as the deformed components gradually relax and convert energy into the displacement of the material until the resulting force returns to zero. It is difficult to measure the distribution of all forces in a complex system. However, their effects can be monitored by measuring the mass flow, which is also the most important parameter to control.

2.3. Experimental set-up

For the experiments performed in this work, the mechanical piston extrusion head (Vitaprint, IRNAS Ltd., Slovenia) was mounted on an analytical balance (XS205, Mettler Toledo, Columbus, Ohio, USA) using a 5 ml syringe (Omnifix, B. Braun, Melsungen, Germany) with an attached nozzle (G21, blunt-end needle – Sterican, B. Braun, Melsungen, Germany) partially immersed in a beaker filled with water, as shown in Fig. 4. The material was extruded into the beaker by controlled depression of the piston. At the same time, the change in deposited mass was recorded on the balance and logged on a personal computer running a Python script (see
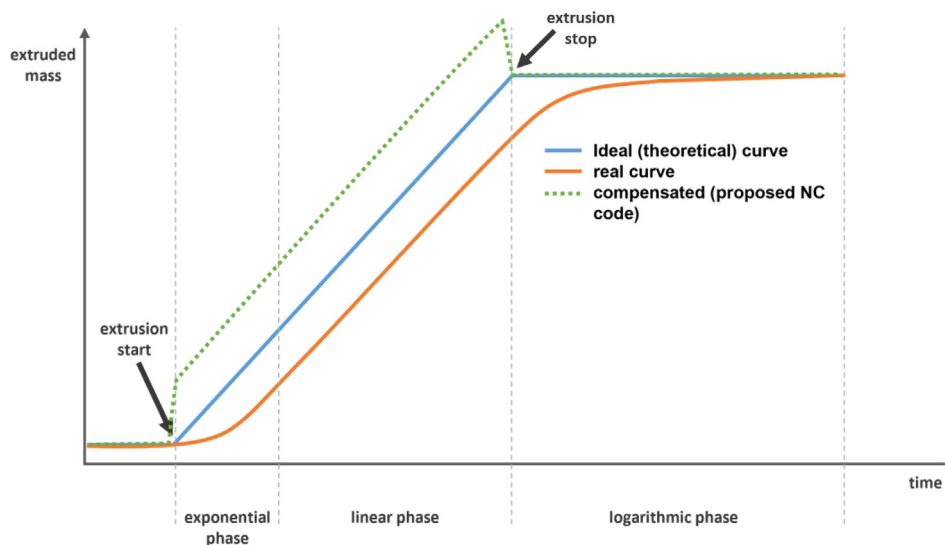

Fig. 3. Comparison of the mass profile for measured and theoretical extrusion. The ideal curve (blue) represents the profile of the extruded mass under ideal conditions, where the displacement of the material is linear to the movement of the piston. The measured curve (orange) represents the measured mass profile when the commands for the ideal curve are executed in an elastic system. The compensated curve (green, dotted) represents the curve that the machine must follow to obtain a measured curve that corresponds to the ideal curve. It increases the extrusion rapidly at the beginning to go directly into the linear phase and then retracts just before the end of the extrusion to bring the mass curve back to zero.
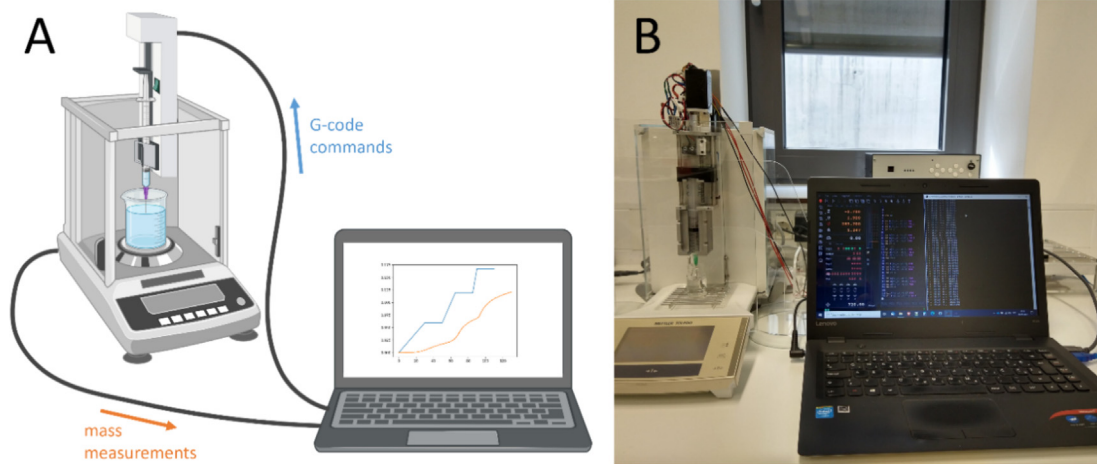
Fig. 4. Visualization of the experimental set-up. **A** shows a schematic and functionality of the set-up, containing the command-extrusion-measurement-analysis loop. **B** shows a photograph of the actual set-up, with the computer (determining and executing the NC code commands and logging data from the weighing scale) and the extruder mounted above the analytical weighing scale, depositing material into a water-filled beaker.

section 2.5). This allowed simultaneous control and monitoring of the extrusion.

For the static configuration (no motion across the ×, y, and z axes), the extrusion component of the total feed rate was extracted using the $\frac{l}{i}$ coefficient as shown in Equation (5). Four materials with different viscosities were used for the tests, including ultrapure water (18.2 MΩ·cm at 25 °C) prepared with an ELGA Purelab water purification system (Veolia Water Technologies, High-Wycombe, UK) and hydrogels of carboxymethylcellulose (CMC) with concentrations of 1%, 2%, and 4% (w/w) CMC (700 kDa, degree of substitution of 0.9, Sigma-Aldrich, Darmstadt, Germany) in ultrapure water, which were soaked overnight at room temperature, mixed vigorously, and centrifuged at 3000 × G for 30 min to remove air bubbles. The extrusion sequence in a single test cycle was set to a constant extrusion rate of 0.1 or 1 mm/min (corresponding to an approximate feed rate of 100 or 1000 mm/min, respectively, for a nozzle diameter of 0.4 mm) and included 8 extrusion steps from 0.05 mm to 0.4 mm piston displacement. The extruded material was weighed during each cycle, and the mass change was compared with the expected values.

2.4. Optimization algorithm

The proposed optimization process aims to reduce the difference between the measured and theoretical (calculated from the NC code) curves by running an auxiliary NC code that includes a ramp and retraction parameter that rapidly deforms the system to the point of linear translation and rapidly relaxes the system to prevent extrusion beyond the point of linear extrusion. Importantly, the retraction matches the ramp value to prevent drawing ambient air into the syringe. Thus, the algorithm (Fig. 5) has two main objectives: a) determine (optimize) the ramp/retraction value and b) generate a new NC code (containing the ramp/retraction parameter) that results in a measured extrusion curve closer to the original theoretical curve.

2.5. The code

The algorithm was programmed using NC code (for the machine instructions) and the Python 3 programming language (for data logging, analysis, and generation of modified NC code). The code used in this work is available on GitHub (link: https://github.com/IRNAS/vitaprint-extrusion-linearization) and can be used

and modified under the GNU general public license v3 (link: https://www.gnu.org/licenses/gpl-3.0.en.html).

The following files are needed to run the algorithm:

- Calibration NC code: basic machine instructions that determine the extrusion steps, rate, and pause time between steps.
- Function library (Python file): a collection of the necessary functions to run the algorithm.
- Calibration script (Python file): containing the main algorithm described in aure 5, which calls functions from the function library file in an intelligible manner.
- Temp file: containing the name of the calibration NC code and the temporary ramp/retreat value.

The algorithm is executed in the following steps:

1. Set the parameters in the temp file (ramp/retreat value and NC code file name) to the desired values (*e.g.*, 0, "calibrate").
2. Load the NC code file into the software that controls the extruder (*e.g.*, PlanetCNC).
3. Run the calibration script and start the NC code when the countdown reaches zero.
4. After a cycle is complete, the Python script creates a new NC code file and modifies the temporary file.
5. Load the new NC code file into the extruder control software and repeat the cycle.

In addition to the above files, another script has been prepared that generates modified NC code files with user-defined ramp/retraction values. This allows the user to shorten the calibration process with an "educated guess" about ramp/retraction values that are closer to the optimum.

2.6. Results variability and evaluation

After reaching the optimum extrusion parameters, a repetition sequence was repeated four times at a feedrate of 1 mm/min, using the material that required the highest ramp/retraction value, namely 2% CMC. The sequence included the following increments of piston movement: 50 μm, 100 μm, 150 μm, 200 μm, 400 μm and a total of 1200 μm, which, considering the syringe and material, translated into projected mass increments of 6 mg, 12 mg, 18 mg, 24 mg, 48 mg and 144 mg respectively. The variability of
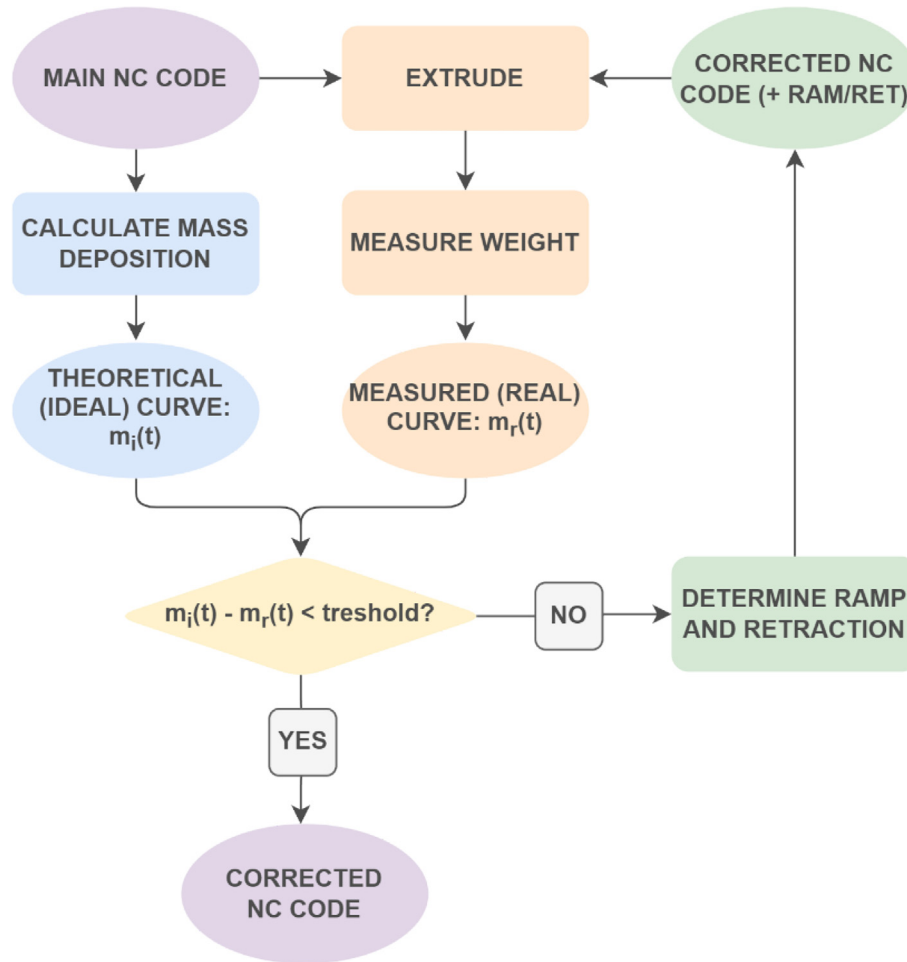
Fig. 5. A schematic of the optimization algorithm. Briefly, based on the difference between the theoretical ($m_i(t)$) and the measured ($m_r(t)$) mass change, the NC code is modified, and the process is repeated until the difference is smaller than a set threshold.

the measured extrusion mass was evaluated and compared to projected values whereas absolute and relative deviations in reference to the total projected mass were considered.

2.7. Rheology measurements

Prior to printing, viscosity was measured for all the gel inks used in this paper: 0% CMC – H_2O; 1% CMC; 2% CMC; and 4% CMC. All measurements were performed with an Anton Paar RheolabQC rheometer with cylinder measurement system CC27-SN25789 according to the ISO 3219 standard. During the measurements the temperature was kept constant at 25 °C and the shear rate (Γ) was increased continuously from 0.01 to 1000 s − 1 with 31 measuring points at every 10 s for a total duration of 310 s. The analysis method and curve fitting according to Carreau-Yasuda [29,30] was used.

2.8. X-ray nanotomography

For better and more accurate graphic representation, resulting scaffolds were scanned using Nano-computed tomography (NanoCT). Images were captured with the 3D X-ray microscope ZEISS Xradia 620 Versa (Carl Zeiss AG, Oberkochen, Germany). Before analysis, the freshly 3D printed scaffolds were crosslinked to stabilize the structure. The measurements were done with a 0.4x objective at 70 kV and 4 W, without an additional filter. Exposure time was set to 0.8 s, and binning was set to 2. These settings

resulted in a voxel size of 24.67 μm. The images were reconstructed using the proprietary ZEISS Xradia software and analyzed using Dragonfly Software (ORS, Montréal, Québec, Canada), which was also used to export the 360° animation of both scaffolds.

3. Results and discussion

3.1. Testing the set-up and initial calibration

Considering the components used in the experimental set-up (5 ml syringes with an inner diameter of 12.5 mm, and G21 needles with an inner diameter of 0.4 mm) and equations (1)–(6), the set-up was tested for a piston displacement rate in the range of 0.1– 1 mm/min, which corresponds to a calculated feed rate (f) of approximately 100–1000 mm/min. Four inks with different viscosities: 0% CMC, 1% CMC, 2% CMC and 4% CMC were used in the experimental calibration with an initial correction (ramp/retraction of the piston in mm) value of 0. The correction value was determined as described in section 2.4 at the end of a measurement cycle and readjusted iteratively until the value change between two cycles was smaller than 0.01 mm. Fig. 6 shows a comparison of the theoretical and measured extrusion curves recorded at an extrusion rate of 1 mm/min (corresponding to a feed rate of 1000 mm/min) using 4% CMC at the different ramp/retraction values.

As the correction value approaches the optimum, the measured curve approaches the theoretical one. However, if the correction
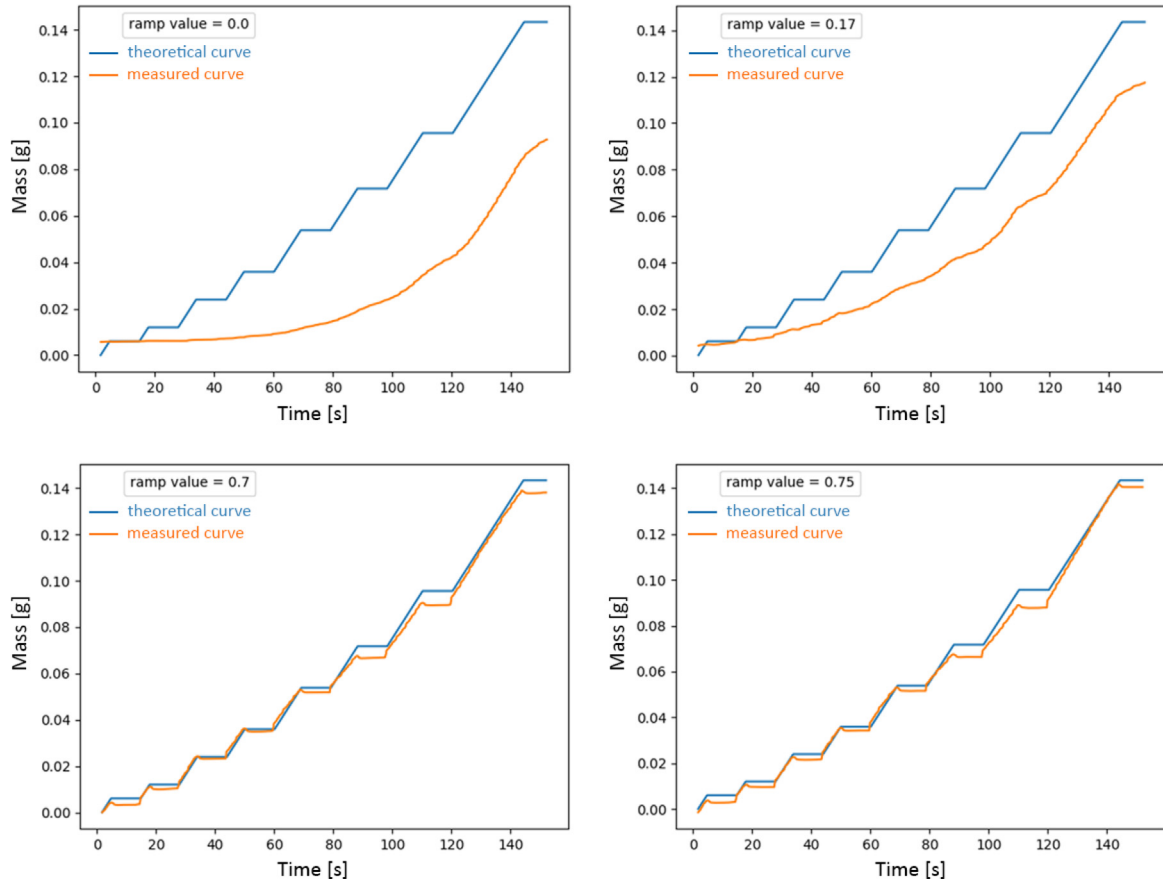
Fig. 6. Progression of measured (compared to calculated) curves as a function of ramp and retraction value. This figure depicts the change of mass extrusion after implementing ramp and retraction with varying values into the NC code. Four iterations of the protocol are shown, corresponding to extrusion of 4% CMC ink at an extrusion rate of 1 mm/min.

value overshoots the optimum, the extrusion steps become exaggerated, resulting in short protrusions at the end of each step which increases the discrepancies between the calculated and measured curves, driving the algorithm to reduce the correction value in the direction of the optimum. The optimum ramp/retraction values for all 4 materials tested, extruded at 0.1 or 1 mm/min rates, were determined as described above and summarized in Table 1.

The results show that the optimum correction value for ramp and retraction depends on both material viscosity and extrusion rate as would be expected when using non-Newtonian fluids. Furthermore, the elastic properties of the syringe and other variables might also contribute cause non-linear behavior of the system. Nevertheless, an optimum correction value was achieved for all tested materials at both extrusion rates. To gain further insight into

material extrusion, the measured correction values were compared to rheological data of the tested materials.

3.2. Integrating rheology data and establishing ramp-shear stress correlations

Fig. 7 shows the measured viscosity of prepared materials and its change with shear rate. With increased CMC concentration
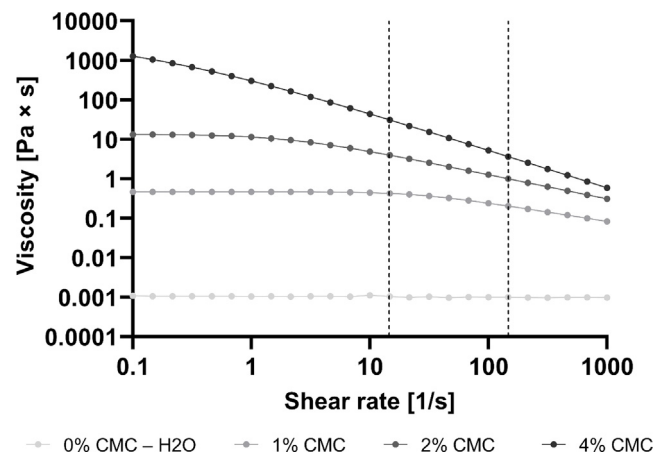
Table 1
Ramp/retraction optimization results based on feed rate and viscosity (CMC concentration). The optimum values were obtained by extruding the listed materials from a 5 ml syringe through a G21 blunt end needle in cycles until the measured mass progression sufficiently resembled the theoretical one as described above and in Fig. 5.

Material composition	Optimized correction value [mm] at f_L = 0.1 mm/min	Optimized correction value [mm] at f_L = 1 mm/min
0% CMC – H_2O	0.09	0.09
1% CMC	0.09	0.53
2% CMC	0.45	1.12
4% CMC	0.54	0.70

Fig. 7. Rheological analysis of materials. The graph depicts the viscosity of aqueous solutions with varying concentrations of CMC (in the range of 0–4%) as a function of shear rate. Pure water exhibits Newtonian behavior with constant viscosity throughout the full range of measured shear rates. With increasing CMC concentration in the solution, the viscosity of respective materials increases, and shear thinning becomes more pronounced.

the viscosity of materials increased exponentially, and shear thinning became apparent at lower shear rates. Within the defined range of extrusion rates (0.1–1 mm/min), marked with the dotted vertical lines in Fig. 7, all materials except pure water exhibit shear thinning behavior.

The obtained rheological data depicted in Fig. 7 allows linking viscosity and shear rate which give the value for shear stress and compare them with the required correction values for piston motion during extrusion (Table 1). The data expressing optimum correction values as a function of shear stress is shown in Fig. 8. Connecting only two points the data is presented as straight lines, though it is reasonable to presume that the curves would take a different shape with additional datapoints. The results suggest that CMC solutions with lower concentrations follow a steep progres-

sion where the extrusion correction value increases more drastically with extrusion rate, however, the correction value change decreases with increasing concentration. Furthermore, the correction value range seems to follow a bell-shaped curve, reaching the highest values using the 2% CMC solution. Pure water was the exception, exhibiting no change in correction value in relation to the shear stress within the measured range. Rheological measurements can roughly predict the extrusion correction value, however, cannot capture the influence of the elasticity of the components involved in the extrusion. Consequently, an iterative approach to extrusion calibration as presented in this work, remains as a necessary and practical method of calibration in extrusion systems with elastic components. As the experimental set-up presented in this work only requires an analytical weighing scale (commonly used in laboratory environments) in addition to the algorithm and a Python running environment, it can be easily adopted by researchers and other professionals that work with syringe-based material displacement, including 3D (bio) printing, microfluidics, *etc.*

The shape and dimensions of the nozzle and the cartridge will significantly impact extrusion. Therefore, the obtained optimization parameters and final NC code will differ from set-up to set-up. However, as long as the principles described in Fig. 2, Fig. 3 and Equations (1)–(11) apply, the optimization algorithm should remain valid when different cartridges and nozzles are used.
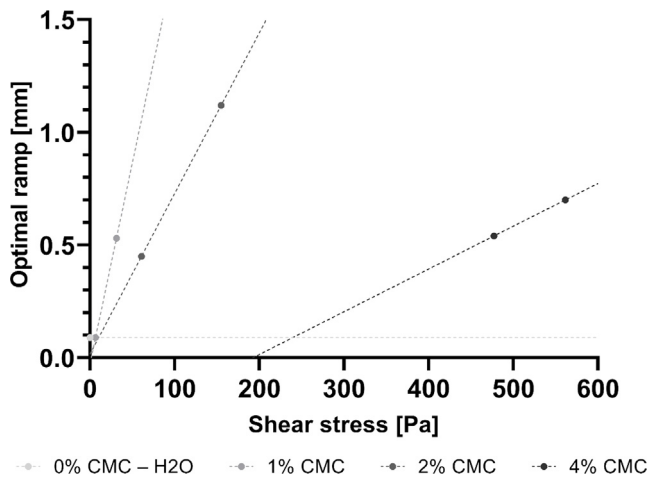
3.3. Translation into practice

To validate the optimization algorithm, the extruder was integrated onto a 3D printer, and printing was performed using an ink with sufficient viscosity to maintain shape fidelity. The ink was prepared with 5% CMC and 0.5% alginate dissolved in 17.5% ethanol (final concentration). CMC and alginate powders were suspended in 1 ml of 70% ethanol and then topped with 3 ml of ultrapure water. An optimization cycle was performed using the developed algorithm, a 5 ml disposable syringe (Omnifix, B. Braun, Melsungen, Germany) and a conical, blunt-ended nozzle (0.25 mm inner diameter; Nordson EFD, Westlake, Ohio, USA). After extru-
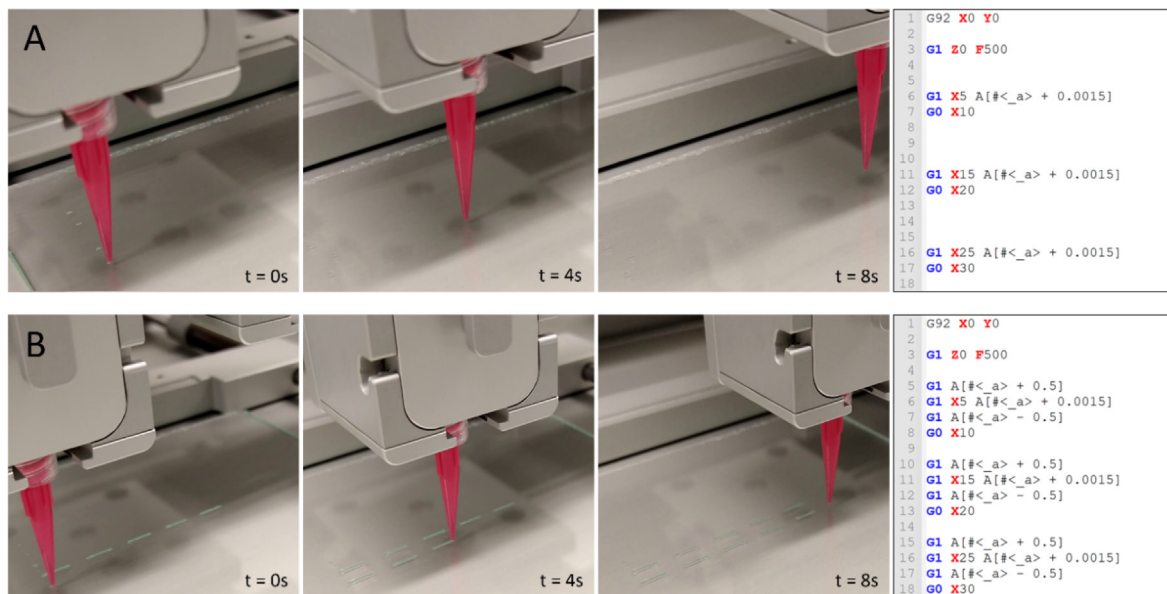

Fig. 8. Optimum correction values as a function of shear stress. Optimum correction values for respective materials as shown in Table 1 are compared to calculated shear stress, calculated from data visible in Fig. 7, maintaining the color coding.

Fig. 9. Validation of optimized extrusion settings. Extrusion patterns of initial and optimized NC codes are shown, printing dashed lines with evenly distributed 5 mm long dashes using a 5% CMC, 0.5% alginate gel dissolved in 17.5% ethanol. **A** shows the initial NC code (right), and the resulting extrusion pattern (left) deposited at after 8 s. Due to the high viscosity and the resulting flow resistance, the pattern without ramp/retraction correction fails to reproduce the determined pattern. **B** shows a corrected NC code and printing of the pattern with a ramp/retraction parameter of 0.5 mm. Here, the printing pattern is perfectly reproduced with repeatable dash length and form. Video footage of the printing is available in the supplementary materials.

sion optimization, the extruder was mounted onto a 3D printer with X, Y and Z axis control and two NC codes were prepared for printing that aimed to print evenly spaced, discrete, 5 mm lines that would form a "dashed path" on subsequent repetitions. The first NC code was prepared without adding ramp and retraction. In contrast, the second NC code included a correction with optimized ramp and retraction values determined during the optimization process. The printing results of the two NC codes are shown in Fig. 9 and are available as a video in the supplementary material. Using a highly viscous material and short extrusion steps, the uncorrected NC code shows almost no material deposition, except for single spots at the starting position, a consequence of the slow run-out during the pauses between printing cycles. In contrast, the corrected NC code produced print patterns that mimicked the specified pattern. In addition, the applied lines showed high reproducibility when the patterns were repeated several times, with a uniform thickness of the applied filament and no discernible run-out.

Furthermore, the algorithm was tested by 3D printing cuboidal $8 \times 8 \times 6$ mm^3 scaffolds with a rectilinear infill pattern using opti-

mized and non-optimized code respectively. Another material was prepared using a 5% CMC and 5% alginate hydrogel supplemented with 1.5% nanofibrillated cellulose to increase material stability when constructing multiple higher structures. The relevant code sections are represented in the Fig. 10 below and the full code is available in the supplementary material.

Nanotomography was used to assess the structure and overall geometry of the 3D printed scaffolds. To allow for stable nanotomography imaging, the scaffolds were crosslinked using a 5%wt $CaCl_2$ solution, warping the geometry and resulting in slightly rounded sides and edges. However, the effect of NC code optimization is clearly visible from the results. The nanotomography reconstructions are shown in Fig. 11. The optimized scaffold has a cuboid shape with hollow channels throughout, while the non-optimized scaffold has an irregular geometry with a seemingly random arrangement of printed fibers. The irregular shape produced using the non-optimized code results from a slow initial extrusion rate, delaying material deposition relative to nozzle movement and causing the nozzle to lose contact with the deposition surface on higher layers. After a critical distance between the nozzle and sub-


```
 4
 5   G1   A[#<_a> +1.81] ;ramp
 6
 7   G1   X8.0      Y0.0      A[#<_a> +0.0130]
 8   G1   X8.0      Y1.333333  A[#<_a> +0.002477]
 9   G1   X0.0      Y1.333333  A[#<_a> +0.0130]
10   G1   X0.0      Y2.666667  A[#<_a> +0.002477]
11   G1   X8.0      Y2.666667  A[#<_a> +0.0130]
12   G1   X8.0      Y4.0       A[#<_a> +0.002477]
13   G1   X0.0      Y4.0       A[#<_a> +0.0130]
14   G1   X0.0      Y5.333333  A[#<_a> +0.002477]
15   G1   X8.0      Y5.333333  A[#<_a> +0.0130]
16   G1   X8.0      Y6.666667  A[#<_a> +0.002477]
17   G1   X0.0      Y6.666667  A[#<_a> +0.0130]
18   G1   X0.0      Y8.0       A[#<_a> +0.002477]
19   G1   X8.0      Y8.0       A[#<_a> +0.0130]
20
21   G1   A[#<_a> -1.81] ;retract
22
```
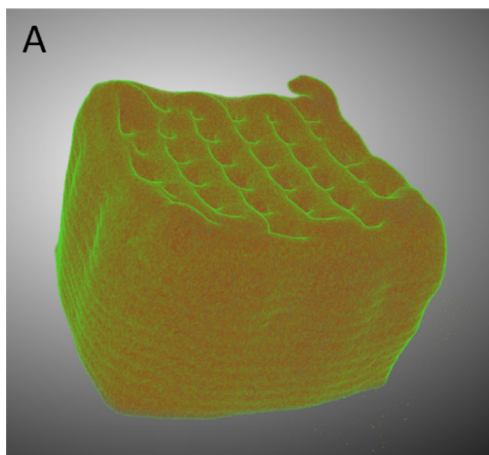
Optimised NC code

```
 4
 5
 6
 7   G1   X8.0      Y0.0      A[#<_a> +0.0155]
 8   G1   X8.0      Y1.333333  A[#<_a> +0.002953]
 9   G1   X0.0      Y1.333333  A[#<_a> +0.0155]
10   G1   X0.0      Y2.666667  A[#<_a> +0.002953]
11   G1   X8.0      Y2.666667  A[#<_a> +0.0155]
12   G1   X8.0      Y4.0       A[#<_a> +0.002953]
13   G1   X0.0      Y4.0       A[#<_a> +0.0155]
14   G1   X0.0      Y5.333333  A[#<_a> +0.002953]
15   G1   X8.0      Y5.333333  A[#<_a> +0.0155]
16   G1   X8.0      Y6.666667  A[#<_a> +0.002953]
17   G1   X0.0      Y6.666667  A[#<_a> +0.0155]
18   G1   X0.0      Y8.0       A[#<_a> +0.002953]
19   G1   X8.0      Y8.0       A[#<_a> +0.0155]
20
21
22
```
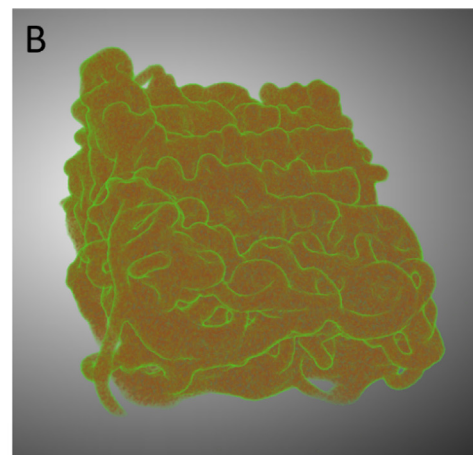
Non-optimised NC code

Fig. 10. Relevant sections of both the optimized and the non-optimized NC codes. Note the ramp and retraction values at the beginning and the end in the optimized NC code.

Fig. 11. Nanotomography reconstructions of both the optimized and non-optimized scaffolds. A) reconstruction of the scaffold printed with the optimized NC code. B) reconstruction of the scaffold printed with the non-optimized NC code. Note the cuboid shape with hollow channels on the optimized scaffold and the seemingly random fiber arrangement on the non-optimized scaffold.

strate is reached, the deposited filament is no longer guided by the printing motion itself and begins to spiral irregularly. A 3D animation of each scaffold reconstruction is available in the supplementary material.

Fig. 12 below shows three slices of each scaffold as scanned by the nanotomograph. The slices are made at the same height of both scaffolds. It can be observed that the channels, although not perfect, are clearly visible on the optimized scaffold, however, on the non-optimized scaffold, a non-regular pattern of channels can be seen.

For direct visual demonstration, four scaffolds of lower height were printed with both optimized and non-optimized NC codes. They were printed in a way that first, the first layer of all the scaffolds was deposited, then, the second layer of all the scaffolds was deposited, etc., until all ten layers were deposited for all four scaffolds. The scaffolds were photographed at the end and are presented in Fig. 13 below.

3.4. Variation of results and possible explanations

Optimization of extrusion parameters was possible for all tested materials. However, certain deviations were observed in the individual test runs, which occurred even when the same NC code was used in several repetitions, as shown in Fig. 14. While the discrepancy between measured (orange data) and theoretical mass (blue data) gradually increases with the total extrusion mass, its proportion to the total extrusion mass drops rapidly and reaches values below 5% at 140 mg.

When even extrusion pressure is maintained during the printing process, movement deceleration due to changes in trajectory (e.g. at angles or serpentines) leads to excessive material deposition. In the set-up described in this work, extrusion is controlled as piston movement along the E axis, which is included in the calculation of the total movement velocity of the print head alongside the X, Y, and Z axes. Thus, deceleration along the nozzle trajectory also decelerates extrusion. Nevertheless, the extrusion response may be slower compared to nozzle motion, depending on the syringe, nozzle and viscoelastic properties of the ink. Developing a setup-specific solution is crucial to overcome this limitation; however, this falls beyond the scope of our work, which focuses on developing an algorithm for optimizing syringe-based extrusion, not limited to 3D printing. Furthermore, several factors may cause the observed variability in results at identical extrusion settings. These include: A) Inhomogeneous viscoelastic properties of the
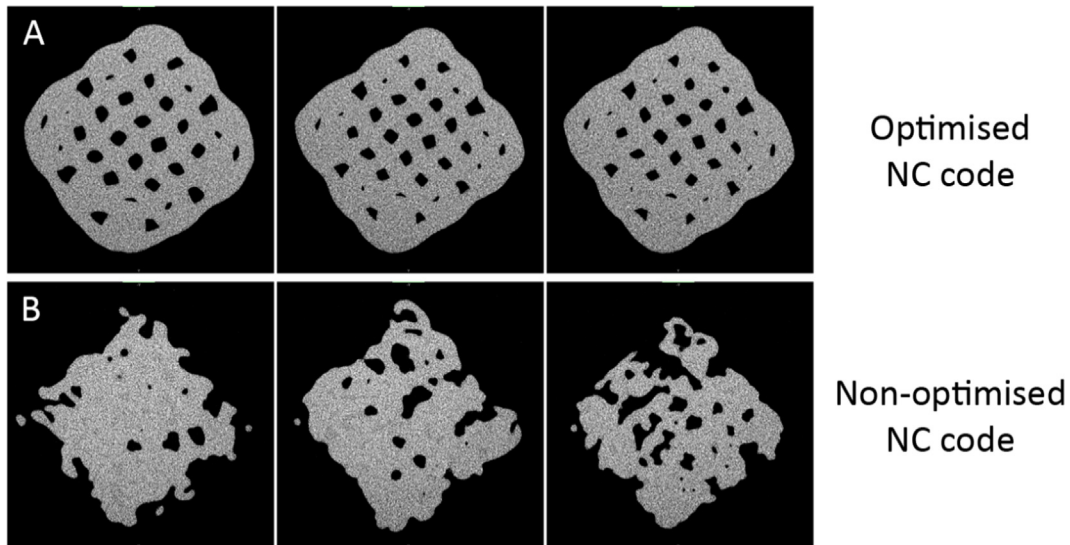

Fig. 12. Slices of the nanotomograms showing internal geometry of the scaffolds. A) three tomography slices of the scaffold printed with the optimized NC code. B) three tomography slices of the scaffold printed with the non-optimized NC code.
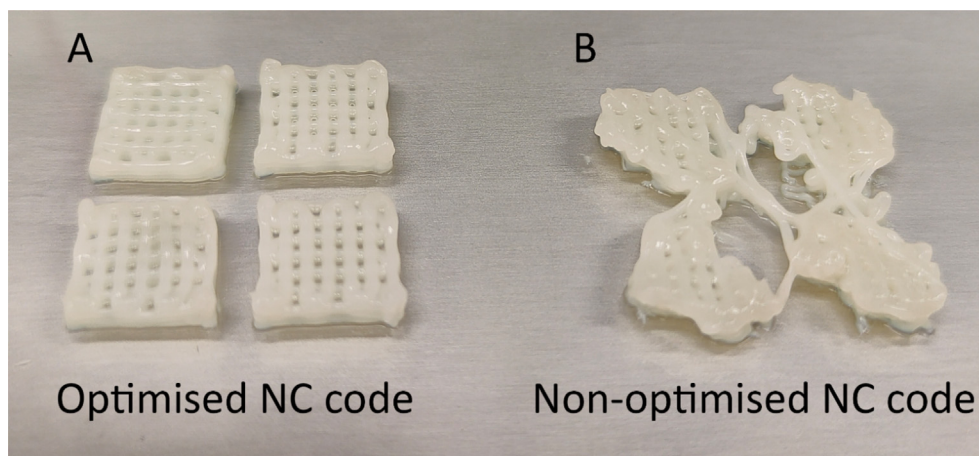

Fig. 13. A photograph of both versions of the four 3D printed scaffolds. A) The scaffolds printed using the optimized NC code. B) The scaffolds printed with the non-optimized NC code.
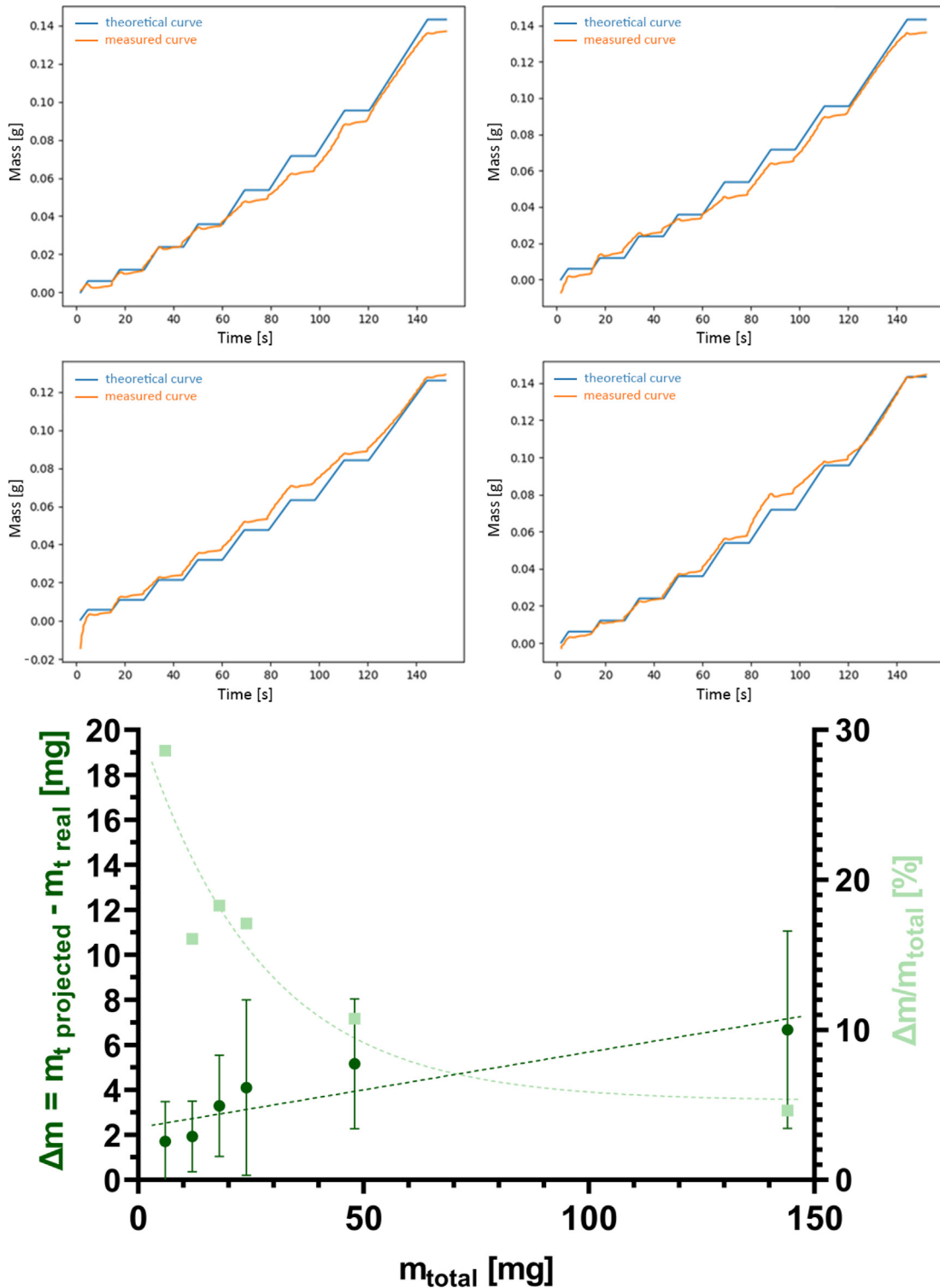
Fig. 14. Variability of measured extrusion under identical experimental conditions. The top four charts show recorded mass progressions of extruding 2% CMC with a ramp/retraction parameter of 1 mm at a feed rate of 1 mm/min with apparent variations in the mass progressions, which is summarized in the bottom chart. The data labelled in dark green shows the average difference between measured and predicted mass at varying increment sizes with a standard deviation of four repetitions shown in the error bars. The data labelled in light green shows how this relates to the cumulative extruded mass of the whole process (top four charts). As the extruded amount of material increases, the relative error decreases.

material. Depending on the components and the preparation process, the extruded material may contain lumps or air bubbles that can significantly affect extrusion. This can be difficult to assess visually, especially when opaque materials and components are used. Therefore, a careful preparation process is essential to ensure proper homogenization and removal of potential contaminants or

air bubbles (*e.g.*, by centrifugation). B) Nonlinear movement of the piston. Especially in low-cost and DIY systems with less precisely manufactured components, the spindles may have a variable pitch that translates into variable piston motion. A possible solution to this type of error (other than replacing the spindle) would be to calibrate the motion along the extrusion axis to compensate
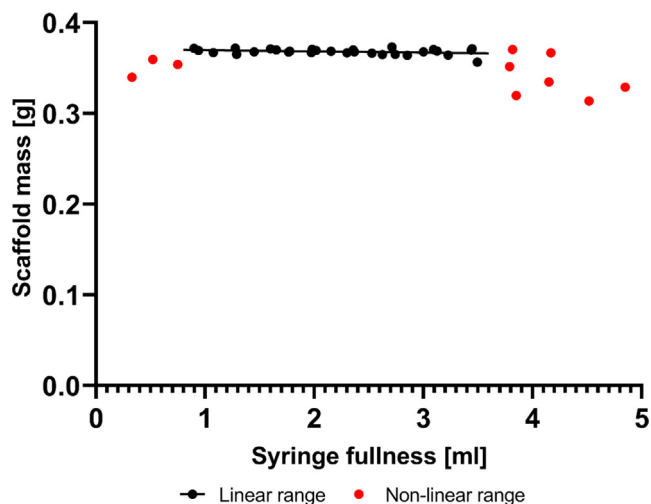
Fig. 15. Printing reproducibility as a function of syringe fullness. Scaffold mass (y-axis) was recorded after repeated 3D printing to empty four variably filled 5 ml syringes, marking syringe fullness at the beginning of each print (x-axis). The first and final prints (in red) show higher variability. However, printing is stable throughout the extrusion of most of the syringe contents with reproducible scaffold mass (black).

for the uneven pitch, which is a topic for future research. C) The amount of material within the cartridge (in this instance, the syringe) relative to its total volume. To evaluate how 'syringe fullness', *i.e.*, the initial position of the piston relative to the syringe cylinder at the start of a print, impacts the results, additional tests were performed in the scope of this work. The scaffolds presented in Figs. 11 and 12 were printed repeatedly to empty a total of four full syringes while comparing the syringe fullness and the mass of the respective scaffolds. The results are depicted in Fig. 15 and show comparable scaffold mass in most instances, apart from the initial (first 1–2 prints after installation of the syringe) and final (when the syringe is almost empty and does not contain sufficient material to complete the scaffolds) prints.

4. Conclusion

This paper presents an empirical algorithmic approach for the rapid adaptation of microextrusion parameters to different materials used in extrusion-based 3D printing devices. The provided algorithm is compatible with a wide range of piston-driven extruders and materials with associated cartridges (*e.g.*, syringes) and nozzles. The operating principle of the proposed algorithm is based on the comparison of the geometrically defined extrusion parameters provided by optional slicing software (the NC code) with the actual extrusion properties of the hardware/material combination used (measured with an analytical balance). The resulting modified NC code file, which compensates for the nonlinear behavior of the material, is based solely on empirical measurements of the extruded mass flow and requires no prior knowledge of the rheological properties of the extruded material. The code required to run the algorithm is freely available through a public GitHub repository (https://github.com/IRNAS/vitaprint-extrusion-linearization). It will continue to be updated in the hope that it will find use in 3D bioprinting and other extrusion-based experiments.

Data availability

The data is made available on github, additional data will be available uppon request.

Declaration of Competing Interest

The authors declare that they have no known competing financial interests or personal relationships that could have appeared to influence the work reported in this paper.

Appendix A. Supplementary material

Supplementary data to this article can be found online at https://doi.org/10.1016/j.matdes.2023.111884.

References

[1] W. Sun, B. Starly, A.C. Daly, J.A. Burdick, J. Groll, G. Skeldon, W. Shu, Y. Sakai, M. Shinohara, M. Nishikawa, J. Jang, D.W. Cho, M. Nie, S. Takeuchi, S. Ostrovidov, A. Khademhosseini, R.D. Kamm, V. Mironov, L. Moroni, I.T. Ozbolat, The bioprinting roadmap, Biofabrication 12 (2) (2020) 022002.

[2] S. Vijayavenkataraman, W.C. Yan, W.F. Lu, C.H. Wang, J.Y.H. Fuh, 3D bioprinting of tissues and organs for regenerative medicine, Adv. Drug Deliv. Rev. 132 (2018) 296–332.

[3] W.L. Ng, C.K. Chua, Y.-F. Shen, Print Me An Organ! Why We Are Not There Yet, Prog. Polym. Sci. 97 (2019).

[4] N. Tsao, 3D Bioprinting 2018–2028: Technologies, Markets, Forecasts, 2018.

[5] L. Banović, B. Vihar, Development of an Extruder for Open Source 3D Bioprinting, Journal of Open Hardware 2 (1) (2018).

[6] J.A. Reid, P.A. Mollica, G.D. Johnson, R.C. Ogle, R.D. Bruno, P.C. Sachs, Accessible bioprinting: adaptation of a low-cost 3D-printer for precise cell placement and stem cell differentiation, Biofabrication 8 (2) (2016) 025017.

[7] A. Maia Chagas, Haves and have nots must find a better way: The case for open scientific hardware, PLoS Biol. 16 (9) (2018) e3000014.

[8] J.M. Pearce, Building Research Equipment with Free, Open-Source Hardware, Science 337 (6100) (2012) 1303–1304.

[9] B. Wijnen, E.J. Hunt, G.C. Anzalone, J.M. Pearce, Open-source syringe pump library, PLoS One 9 (9) (2014) e107216.

[10] E. Dolgin, How to start a lab when funds are tight, Nature 559 (7713) (2018) 291–293.

[11] N. Bessler, D. Ogiermann, M.-B. Buchholz, A. Santel, J. Heidenreich, R. Ahmmed, H. Zaehres, B. Brand-Saberi, Nydus One Syringe Extruder (NOSE): A Prusa i3 3D printer conversion for bioprinting applications utilizing the FRESH-method, HardwareX 6 (2019) e00069.

[12] A.S. Booeshaghi, E.d.V. Beltrame, D. Bannon, J. Gehring, L. Pachter, Principles of open source bioinstrumentation applied to the poseidon syringe pump system, Scientific Reports 9(1) (2019) 12385.

[13] V. Klar, J.M. Pearce, P. Kärki, P. Kuosmanen, Ystruder: Open source multifunction extruder with sensing and monitoring capabilities, HardwareX 6 (2019) e00080.

[14] K. Pusch, T.J. Hinton, A.W. Feinberg, Large volume syringe pump extruder for desktop 3D printers, HardwareX 3 (2018) 49–61.

[15] J.W. Tashman, D.J. Shiwarski, A.W. Feinberg, A high performance open-source syringe extruder optimized for extrusion and retraction during FRESH 3D bioprinting, HardwareX 9 (2021) e00170.

[16] M. Wagner, A. Karner, P. Gattringer, B. Buchegger, A. Hochreiner, A super low-cost bioprinter based on DVD-drive components and a raspberry pi as controller, Bioprinting 23 (2021) e00142.

[17] C.J. Forman, H. Tomes, B. Mbobo, R.J. Burman, M. Jacobs, T. Baden, J.V. Raimondo, Openspritzer: an open hardware pressure ejection system for reliably delivering picolitre volumes, Sci. Rep. 7 (1) (2017) 2188.

[18] R.E.B. Fitzsimmons, M.S. Aquilino, J. Quigley, O. Chebotarev, F. Tarlan, C.A. Simmons, Generating vascular channels within hydrogel constructs using an economical open-source 3D bioprinter and thermoreversible gels, Bioprinting 9 (2018) 7–18.

[19] A.F. Bonatti, I. Chiesa, G. Vozzi, C. De Maria, Open-source CAD-CAM simulator of the extrusion-based bioprinting process, Bioprinting 24 (2021) e00172.

[20] F. Perin, E. Spessot, A. Famà, A. Bucciarelli, E. Callone, C. Mota, A. Motta, D. Maniglio, Modeling a Dynamic Printability Window on Polysaccharide Blend Inks for Extrusion Bioprinting, ACS Biomater Sci. Eng. 9 (3) (2023) 1320–1331.

[21] Z. Fu, V. Angeline, W. Sun, Evaluation of Printing Parameters on 3D Extrusion Printing of Pluronic Hydrogels and Machine Learning Guided Parameter Recommendation, Int J Bioprint 7 (4) (2021) 434.

[22] B.R. Maciel, K. Baki, C. Oelschlaeger, N. Willenbacher, The Influence of Rheological and Wetting Properties of Hydrogel-based Bio-Inks on Extrusion-based Bioprinting Chem, Ing. Tech. 94 (3) (2022) 393–401.

[23] E. Sodupe-Ortega, A. Sanz-Garcia, A. Pernia-Espinoza, C. Escobedo-Lucea, Accurate Calibration in Multi-Material 3D Bioprinting for Tissue Engineering, Materials (2018).

[24] I.M. Syntouka, P.E. Riches, G. Busby, A. Kazakidi, R. Owen, R. de Borst, J. Reese, C. Pearce, Flow simulation of a natural polymer in a syringe-needle delivery device, 6th European Conference on Computational Mechanics, 2018, pp. 2938-2949.

[25] S.J. Muller, E. Mirzahossein, E.N. Iftekhar, C. Bacher, S. Schrufer, D.W. Schubert, B. Fabry, S. Gekle, Flow and hydrodynamic shear stress inside a printing needle during biofabrication, PLoS One 15 (7) (2020) e0236371.

[26] Z. Żołek-Tryznowska, Rheology of Printing Inks, Printing on Polymers (2016) 87–99.

[27] T.G. Mezger, The Rheology Handbook: For users of rotational and oscillatory rheometers, Vincentz Network GmbH & Co KG2020.

[28] A. Vázquez-Quesada, A. Mahmud, S. Dai, M. Ellero, R.I. Tanner, Investigating the causes of shear-thinning in non-colloidal suspensions: Experiments and simulations, J. Nonnewton. Fluid Mech. 248 (2017) 1–7.

[29] M.C. García, M.C. Alfaro, N. Calero, J. Muñoz, Influence of polysaccharides on the rheology and stabilization of α-pinene emulsions, Carbohydr. Polym. 105 (2014) 177–183.

[30] M. Milojević, L. Gradišnik, J. Stergar, M. Skelin Klemen, A. Stožer, M. Vesenjak, P. Dobnik Dubrovski, T. Maver, T. Mohan, K. Stana Kleinschek, U. Maver, Development of multifunctional 3D printed bioscaffolds from polysaccharides and NiCu nanoparticles and their application, Appl. Surf. Sci. 488 (2019) 836–852.